

# Identifying Correlations in Precessing Gravitational-Wave Signals with Machine Learning

Karen Kang,<sup>1</sup> Simona J. Miller,<sup>2,3</sup> Deborah Ferguson,<sup>4,5</sup> and Katerina Chatziioannou<sup>2,3</sup>

<sup>1</sup>*Department of Physics and Astronomy, Amherst College, Amherst, MA 01002, USA*

<sup>2</sup>*Department of Physics, California Institute of Technology, Pasadena, California 91125, USA*

<sup>3</sup>*LIGO Laboratory, California Institute of Technology, Pasadena, California 91125, USA*

<sup>4</sup>*Center for Gravitational Physics and Department of Physics, The University of Texas at Austin, Austin, TX 78712*

<sup>5</sup>*Department of Physics, University of Illinois Urbana-Champaign, Illinois 61801, USA*

Binary black hole (BBH) spins provide unique and important insights into the formation environments, evolutionary history, and dynamics of these objects. We would like to gain a better understanding of the merger-dominated gravitational-wave (GW) signals from highly massive highly spinning BBH systems, which are prone to spurious measurements due to their very short duration and low bandwidth. Astrophysical parameters are extracted from GW signals by match-filtering with numerical relativity (NR) waveform templates. The degeneracies in waveforms, where dissimilar parameters yield similar waveforms, further complicates source identification. Using machine learning, we visualize these degeneracies in the seven-dimensional BBH intrinsic-parameter space and develop models to quantify parameter correlations. We also propose enhancing existing mismatch-prediction neural networks with higher order modes and precession effects, thereby refining our ability to model – and thus appropriately account for – these degeneracies in highly massive, spinning systems.

## I. INTRODUCTION

GW190521 ( $M \sim 150\odot$ ) is the heaviest BH binary detected to date and one of the few BBHs measured to be highly precessing. It is the first strong observational evidence of intermediate-mass BH (IMBH), which is believed to be the missing link for explaining the formation of supermassive BHs [1]. The detected waveform is dominated by the merger phase where effects of precession remain elusive. In the ongoing LIGO’s fourth observing run (O4) as well as in the advent of the space-based Laser-Interferometer Space Antenna (LISA) and the ground-based Einstein Telescope (ET), we expect to observe large sample of events similar to GW190521 as a result of increased detector sensitivity. Spin configurations reveal insights into the orbital dynamics of compact progenitors and therefore help illuminate the formation channels of BH mergers in the pair-instability (PI) mass gap and aid population modeling of BBHs.[1, 2].

To effectively extract astrophysical information from these signals, it is essential to understand phenomenologically how the GW waveform varies based on BBH parameters, especially for highly massive, precessing systems. Due to the inverse mass-frequency relationship, GW signals from massive binaries would leave few cycles in the LIGO sensitive band. Inherent degeneracies, when multiple parameters produce similar waveforms, further complicates data interpretation. We aim to respond to signals from such systems with maximal accuracy, which requires a thorough understanding of the measurability of spin parameters from detected waveforms. Spin parameters, in particular, which are traditionally derived from the inspiral phase, are poorly constrained for these merger-dominated signals [3]. There is evidence, however, that the merger-phase can contain some information about the preceding orbital dynamics [4]. In light of the existing gaps in our understanding of how precession imprints GW signals, if LIGO purports the detection of significant precession effects, it is crucial to evaluate how parameter degeneracies could be skewing our measurements and interpretation.

In this paper, we outline our method of systematically mapping correlations in the BBH waveform parameter space. We evaluate the degeneracy between waveforms with the mismatch metric  $\mathcal{MM}$  [5, 6], defined as:

$$\mathcal{MM} = 1 - \max_{t,\phi} \mathcal{O}[h_1, h_2] \equiv 1 - \max_{t,\phi} \frac{\langle h_1 | h_2 \rangle}{\sqrt{\langle h_1 | h_1 \rangle \langle h_2 | h_2 \rangle}} \quad (1)$$

where we take the normalized inner product of the frequency domain strains  $h_1, h_2$ , optimized over time

and phase, to be the overlap of two waveforms,

$$\langle h_1 | h_2 \rangle = 2 \int_{f_0}^{\infty} \frac{h_1^* h_2 + h_1 h_2^*}{S_n} df$$

under  $S_n$ , the one-sided power spectral density of the detector. The metric  $\mathcal{MM}$  is normalized to 1, with  $\mathcal{MM} = 0$  representing two completely identical waveforms. We identify the correlations between BBH parameters by studying the regions in the waveform parameter space that have low mismatches between each other.

Quasi-circular BBHs are distinctively characterized by their component masses and spin vectors. However, since BBH simulations in vacuum are scalable by the total mass, we only need to utilize the mass ratio  $q$ , or symmetric mass ratio,  $\eta$ , to describe the system:

$$\begin{aligned} q &= \frac{m_1}{m_2} & 1 \leq q \\ \eta &= \frac{m_1 m_2}{(m_1 + m_2)^2} = \frac{q}{(q + 1)^2} & 0 \leq \eta \leq 0.25 \end{aligned} \quad (2)$$

The BBH waveform parameter space is this seven-dimensional, with parameters  $\lambda = \eta, \mathbf{a}_1, \mathbf{a}_2$ , consisting of a scalar and two three-dimensional vector quantities with  $x, y, z$  components. The  $z$ -axis denotes the direction of the system’s orbital angular momentum  $\hat{\mathbf{L}}$ . By excluding the poorly-measured spin azimuthal angles, we can reduce the parameter space to five dimensions by parameterizing the spin vectors  $\mathbf{a}_1, \mathbf{a}_2$  in terms of spin magnitudes  $a_1, a_2$  and tilt angles  $\theta_1, \theta_2$  (azimuthal tilt angle relative to  $\hat{\mathbf{L}}$ ), as illustrated in Fig.1.

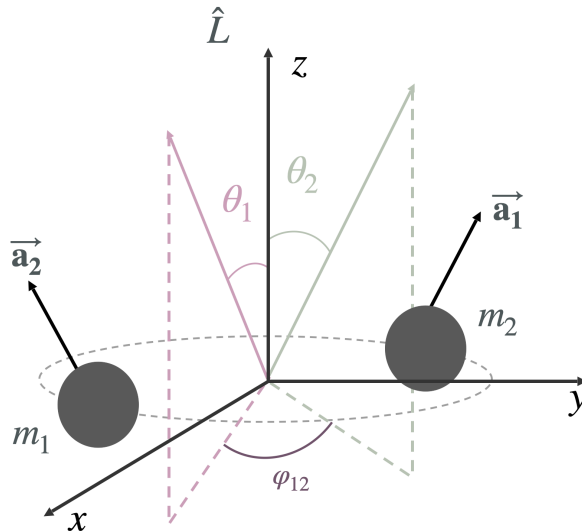


FIG. 1: Configuration of precessing binary black holes relative to the orbital angular momentum  $\hat{\mathbf{L}}$  along  $z$ .

In order to map correlations within the BBH waveform parameter space, we make use of the neural network `mismatch_prediction` presented in Ferguson [7] (detailed in Section III C) to rapidly predict mismatches between waveforms; see Eq. (1). Then we apply “walker algorithm” that systematically explores the degenerate regions, i.e. low mismatch values, in some chosen degrees of freedom, and interpret the path taken by the walker. The rest of the paper is organized as follows. In Section II, we establish preliminary background on effective waveform parameters, known degeneracies, and the neural network used for parameter space generation. Then we present in Section III the mapping algorithm we developed for identifying parameter correlations, followed by preliminary results in Section IV, which includes mapping in two, three, and five degrees of freedom, verifying the effectiveness of our method.

## II. BACKGROUND

### A. Effective Spin Parameters

It is difficult to infer component spin parameters from GW signals; we instead use “effective” spin parameters,  $\chi_{\text{eff}}$  and  $\chi_p$ , which show up in waveforms to leading order. The effective inspiral spin  $\chi_{\text{eff}}$  is the mass-weighted average of the components of the BBH’s spins aligned with the system’s angular momentum

$$\chi_{\text{eff}} = \frac{m_1 a_1 \cos(\theta_1) + m_2 a_2 \cos(\theta_2)}{m_1 + m_2} \quad -1 \leq \chi_{\text{eff}} \leq 1 \quad (3)$$

The effective precession spin can be modeled with a single parameter  $\chi_p$ , which is defined to be the mass-weighted in-plane spin component that contributes to precession of the orbital plane at some (arbitrary) instant during the inspiral phase [8].

$$\chi_p = \max \left( a_1 \sin(\theta_1), \frac{4m_2^2 + 3m_1 m_2}{4m_1^2 + 3m_1 m_2} a_2 \sin(\theta_2) \right) \quad 0 < \chi_p < 1 \quad (4)$$

In terms of the mass and spin parameters, we can rewrite  $\chi_p$  as

$$\chi_p = \max \left( \sqrt{a_{1x}^2 + a_{1y}^2}, \frac{4 + 3q}{4q^2 + 3q} \sqrt{a_{2x}^2 + a_{2y}^2} \right) \quad (5)$$

For more massive systems, where the merger and ringdown phases contribute significantly to the signal, the GW waveforms exhibit more complex morphologies, especially in systems with precession effects that result in waveforms of modulating amplitudes.

### B. Spin-Mass Degeneracy

The  $\chi_{\text{eff}} - \eta$  degeneracy is well-established and falls out naturally from the Post-Newtonian (PN) waveform expansion [9–11]:

$$\psi_{1.5} = (\pi \mathcal{M} f)^{-2/3} \psi$$

where  $\chi_a = (\chi_{z,1} - \chi_{z,2})/2$  and

$$\psi = \eta^{-3/5} \left[ \frac{(113 - 76\eta)\chi_{\text{eff}} + 76\delta\eta\chi_a}{128} - \frac{3\pi}{8} \right]$$

Previous studies have shown that the linear relationship

$$\beta = \frac{113 - 76\eta}{12} \chi_{\text{eff}} + \frac{76\delta\eta}{12} \chi_a$$

is better measured than the effective spin and reduces waveform degeneracies resulting from the mapping between  $(\eta, \psi)$  and  $(q, \chi_{\text{eff}})$  [12]. Fig. 2 provides a visualization of the degeneracies between the parameters  $\chi_{\text{eff}}$  and  $\eta$  in the case where BH spins are aligned/anti-aligned with the orbital angular momentum, with varying mass ratios. We use this linear degeneracy to verify the effectiveness of our mapping algorithm — when the correlation in the parameter space is projected onto the  $\chi_{\text{eff}} - \eta$  plane, it should (at least approximately) follow this linear form.

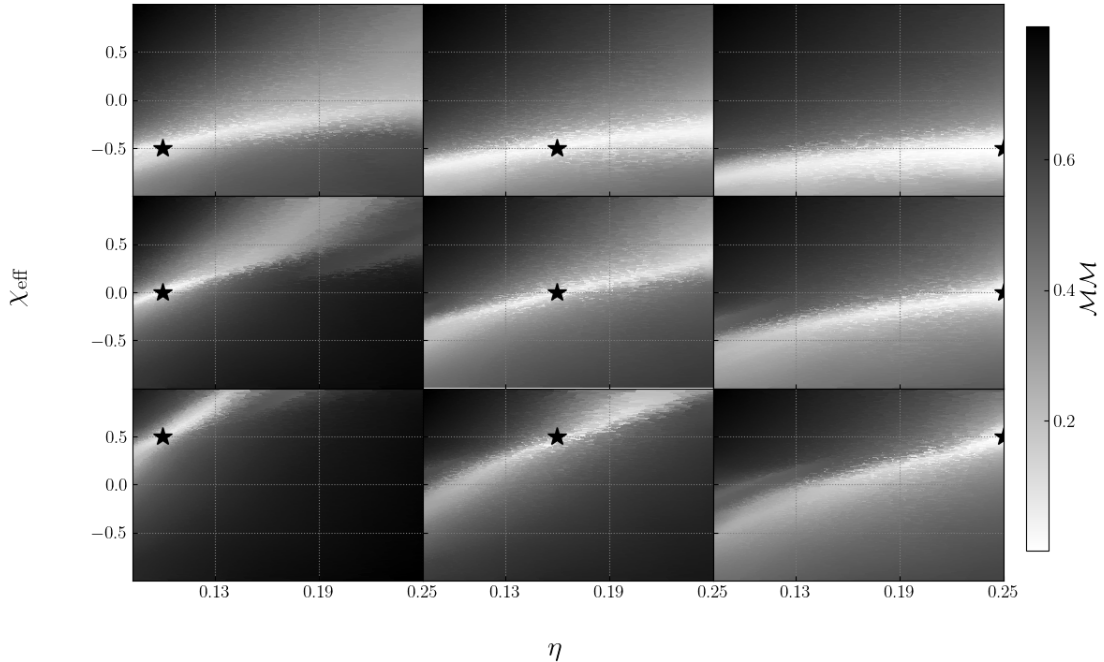


FIG. 2: Mismatch between waveform of reference binary (black dot) and of other binaries throughout the parameter space plotted as  $\chi_{\text{eff}}$  vs.  $\eta$ . From left to right, the reference simulation has  $\eta = 0.1, 0.16, 0.25$ . From top to bottom, the reference has  $\chi_{\text{eff}} = -0.5, 0, 0.5$ . Adapted from Fig. 11 in Ferguson [7].

### C. Generating Waveform Parameter Space with Neural Network

#### 1. Network Overview

In the existing `mismatch_prediction` network, the mismatch is computed on a flat noise curve at  $f_{\text{ref}} = 1840$  Hz using PyCBC [13] and LALSimulation[14]. The original network is trained on a total number of 1885 waveforms, split randomly into training, development, and test sets with ratios of 0.8/0.1/0.1, using  $l = 2, m = 2$  modes to simplify phase alignment for mismatch calculation. The starting frequency  $f_0$  is set at 20 Hz to include 95% of waveforms in the SXS public catalog, corresponding to a detector frame mass of  $100 M_{\odot}$ . The network consists of 15 hidden layers, each with 56 nodes, chosen from models in TensorFlow and Keras library to achieve lowest development error. It was trained using an Adam optimizer with a learning rate of 0.001 for 1000 epochs and batch size of 16.

The network architecture is visualized in Fig. 4. For a comprehensive discussion and detailed analysis of the network’s accuracy and other specifications, refer to Ferguson [7].

#### 2. Parameter Space Generation

We sample uniformly over the generation parameters  $\eta$  and spin vectors  $\mathbf{a}_1, \mathbf{a}_2$  and use the network to predict the mismatch between the reference waveform of specified parameters and the waveform resulting from randomly picked generation parameters. When mapping correlations, we generate a parameter space of  $N = 10,000$  points. Since we are mapping within the “degenerate region” of the parameter space, we adjust the mismatch threshold to include about 1 – 2% of the total number of points.

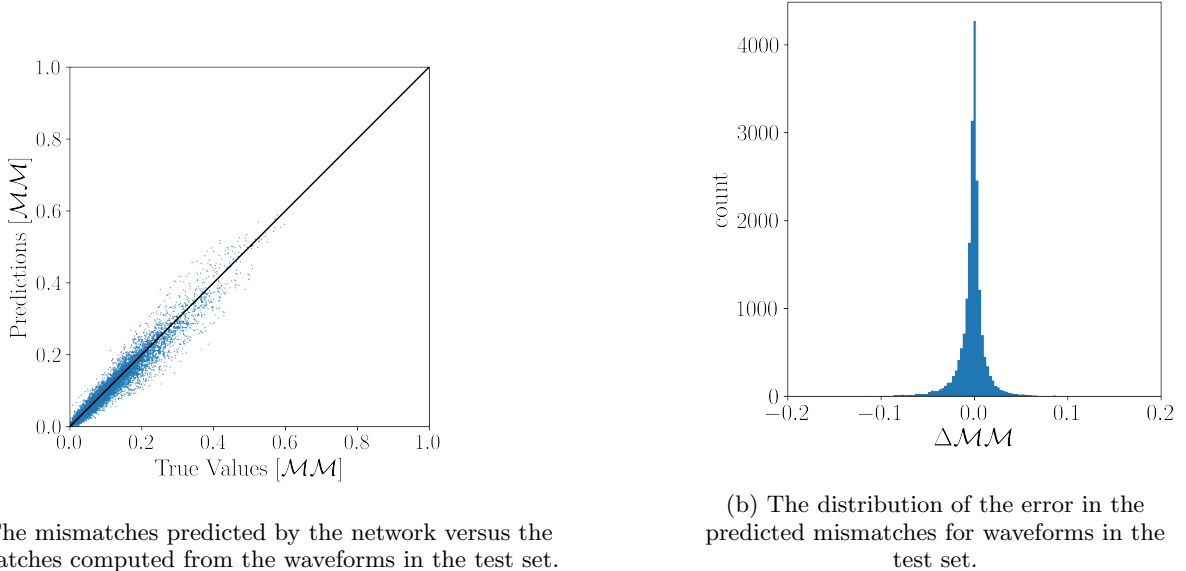


FIG. 3: The error in the predicted mismatch for the waveforms in the test set.

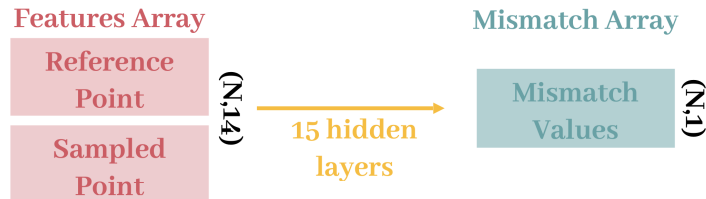


FIG. 4: Diagram showing input (features array of two systems  $\lambda = \{\eta, a_{1x}, a_{1y}, a_{1z}, a_{2x}, a_{2y}, a_{2z}\}$ ) and the output (the mismatch between waveforms) for generating the waveform parameter space using `mismatch.prediction`.

### 3. Including Higher Order Modes (HoMs)

We updated the current network to include higher order modes using waveform model `NRSur7dq4`, which is the only model calibrated to numerical simulations of precessing BH binaries, including the full six-dimensional spin degrees of freedom and higher harmonics [3, 15]. `NRSur7dq4` is trained on NR simulations with mass ratios  $q \leq 4$  and spin magnitudes  $a_1, a_2 < 0.8$ . The model extrapolates to  $q \leq 6$  and  $a_1, a_2 < 1$ . We randomly sampled 2000 points in the parameter space to generate waveforms for training the network. The coverage of the parameter space is shown in Fig. 5.

Since this study is motivated by highly massive, precessing BBH systems, we adjusted the detector frame mass to be  $270 M_\odot$  and distance to be 5000 Pc, corresponding to maximum posterior values of GW190521. Following the same training routine from the published model, the current network for GW190521-like systems has a training error of 0.0081 and a development error of 0.0131, both at a lower value than the original network. The error in the updated high-mass network is shown in Fig. 3b. This reduction in error is likely due to the shorter duration of the waveforms, as almost all of the true mismatch values fall under 0.6. Since we are using models to train the network, the coverage of the parameter space is more uniform compared to the SXS catalog, which may also contribute to the lower uncertainty.

In this paper, we use the original published network trained on SXS catalog waveforms to generate

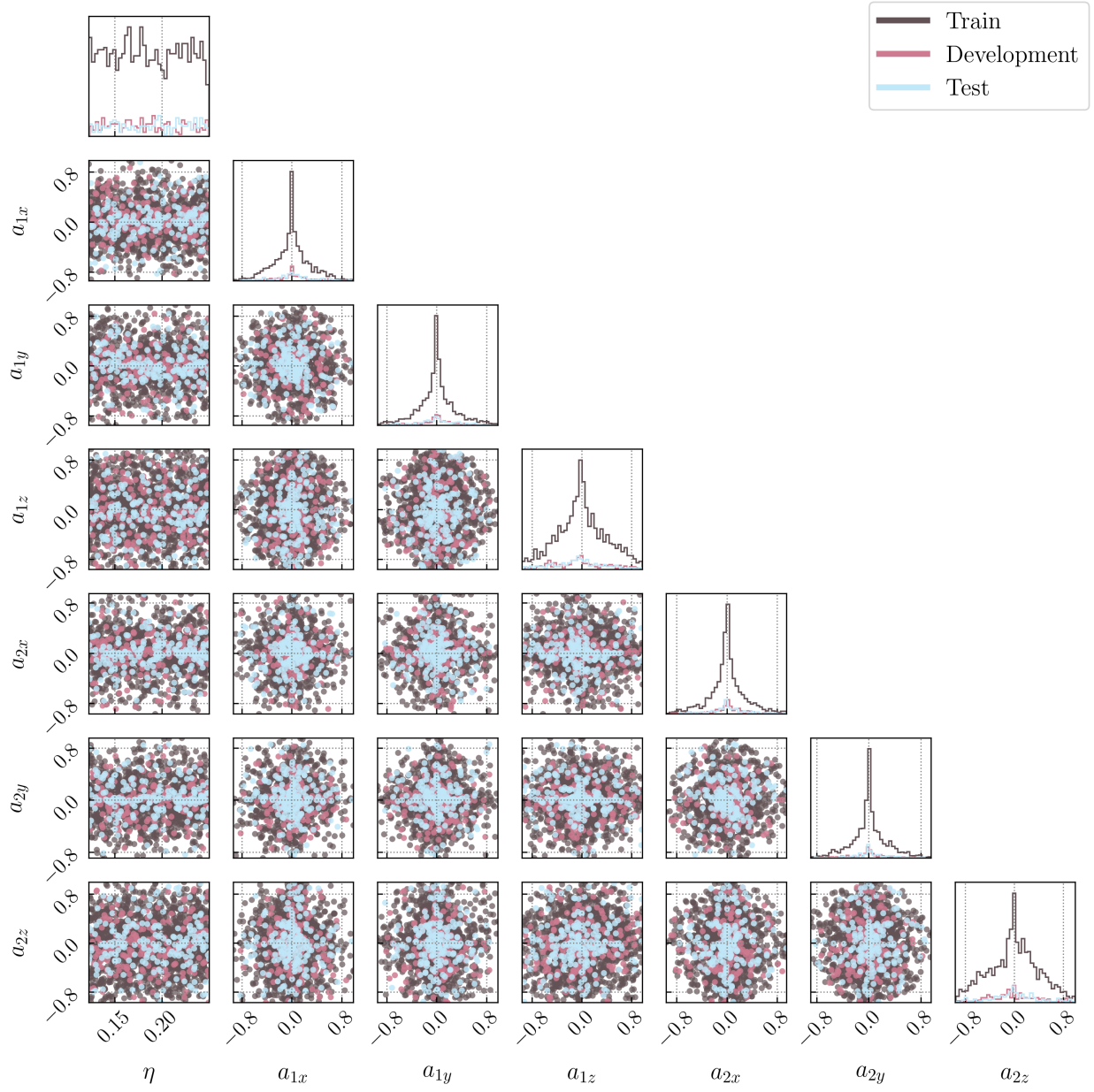


FIG. 5: Coverage of the parameter space by NR waveform models in training (brown), development (pink), and test sets (blue).

the waveform parameter space [7]. We plan to train a low-mass network using phenomenological model IMRPhenomXPHM including HoMs, and run analysis across all three networks trained on different detector frame masses to compare correlation recovered.

### III. MAPPING ALGORITHM

#### A. Object-Oriented Approach: BBH, ParameterSpace, MapDegeneracyND

Our approach leverages an object-oriented architecture, primarily structured around three central classes:

- **BBH**: represents an individual binary black hole (BBH) system.
  - **Attributes**: Intrinsic properties such as mass ratios ( $q, \eta$ ), spin vectors, and spin angles. Effective parameters such as  $\chi_{\text{eff}}, \chi_p$
  - **Instantiation**: Parameters can be specified directly  $\lambda = \{\eta, a_{1x}, a_{1y}, a_{1z}, a_{2x}, a_{2y}, a_{2z}\}$  or generated randomly.
- **ParameterSpace**: consists of BBH objects
  - **Instantiation**: Randomly samples parameter space of chosen dimensions to initialize BBHs and calculate the mismatch at each point with respect to reference simulation
  - **Visualization**: Produces 2D/3D plots for visualizing the degeneracies in the parameter space
- **MapDegeneracyND**: runs mapper in continuously generated **ParameterSpace** until termination condition is reached.
  - **Instantiation**: initializes with reference simulation and mapping controls like fit method, sample size, and mismatch threshold masks.
  - **Functional Flow**: Constructs the **ParameterSpace** and statistically models the space to identify regions of degeneracy.
  - **Execution**: Runs the core loop that progressively navigates the parameter space based on set conditions and statistical fits.

#### B. Algorithm Outline

We assessed a range of statistical models to identify correlations within the parameter space. Notably, the Bayesian Gaussian Modeling (GMM) and the Principal Component Analysis (PCA) proved to be the most effective. We are able to directly identify the direction of the largest spread of distribution, which corresponds to the least variance. The Bayesian Gaussian Fitting achieves this through eigen-decomposition of the covariance matrix, while the Principal Component Analysis transforms data points along the principal components using singular-value decomposition (SVD). Despite the procedural differences in finding this direction, the two methods yield comparable results (see Appendix B).

Since it requires the full features array  $\lambda = \{\eta, a_{1x}, a_{1y}, a_{1z}, a_{2x}, a_{2y}, a_{2z}\}$  to generate mismatch of a waveform in a given parameter space, we add in a K-nearest neighbor (KNN) approximation when choosing the next point along the principal direction: we regenerate the parameter space take steps along the mapping direction, each step (proposed point) is ranked through KNN, and we regenerate the parameter space using the highest-ranking (closest) point along the direction.

### IV. CORRELATION RECOVERY

We first verified the accuracy of the mapping algorithm in a two-dimensional setting where  $\chi_{\text{eff}} - \eta$  degeneracy is well-understood. As we progressed to higher dimensions incorporating more intrinsic parameters, the correlations in these spaces remain uncharted due to measurement challenges and the absence of analytical solutions. To ensure our algorithm’s effectiveness in these complex scenarios, we transformed the mapper’s path back onto the  $\chi_{\text{eff}} - \eta$ , checking that the correlations identified are consistent with established patterns.

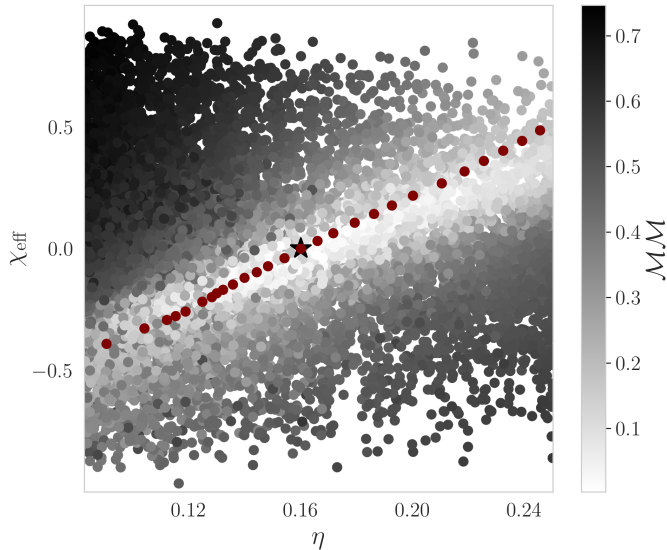


FIG. 6: Path calculated by the walker algorithm for starting reference point at  $\lambda = [0.16, 0, 0, 0, 0, 0, 0]$  plotted in red. The background data points are simulations with predicted mismatch with respect to the starting reference point.

#### A. Two-dimensional Analysis: Effective Spin and Symmetric Mass Ratio

We started with testing the mapping algorithm on the  $\chi_{\text{eff}} - \eta$  plane. We started at  $\eta = 0.16, \chi_{\text{eff}} = 0$  and mapped to both directions (by adding and subtracting the direction vector) until boundary is reached. The resulting path is shown in Fig. 6, which overlaps with the linear degeneracy.

#### B. Three-dimensional Analysis: Mass Ratio with Aligned Spins

We then proceeded on testing the mapping with an extra dimension: using the mass ratio  $q$  and aligned component spins  $a_{1z}, a_{2z}$ . Since Eq. 3 can be written as

$$\chi_{\text{eff}} = \frac{q a_{1z} + a_{2z}}{q + 1}$$

we would like to map the correlation between the parameters  $q, a_{1z}, a_{2z}$  and verify if the projection matches the linear degeneracy on  $\chi_{\text{eff}} - \eta$  plane. We set the initial reference parameters the same as the nine simulations in Fig. 2, where  $\eta = 0.1, 0.16, 0.25$  and  $\chi_{\text{eff}} = -0.5, 0, 0.5$ . This is an intermediate step for verifying the effectiveness of our mapping algorithm. We are attempting to recover the correlation between effective parameters  $\chi_{\text{eff}} - \eta$  by mapping intrinsic BBH  $q, a_{1z}, a_{2z}$ . The three-dimensional mapping analysis using mass ratio  $q$  and aligned spins  $a_{1z}, a_{2z}$  provided promising results. The mapping was able to identify correlations that are in excellent agreement with the expected linear degeneracy on the  $\chi_{\text{eff}} - \eta$  plane. Given the success of this intermediate step, our next phase of work will focus on incorporating additional spin parameters to better model precession effects.

#### C. Five-dimensional Analysis: Mass Ratio, Spin Magnitudes, and Spin Angles

Once we confirmed that the algorithm is able to map in three dimensions  $q, a_{1z}, a_{2z}$ , we included spin tile angles  $\theta_1, \theta_2$  and used spin magnitudes  $a_1, a_2$  instead of aligned spin components. We are thus mapping in five

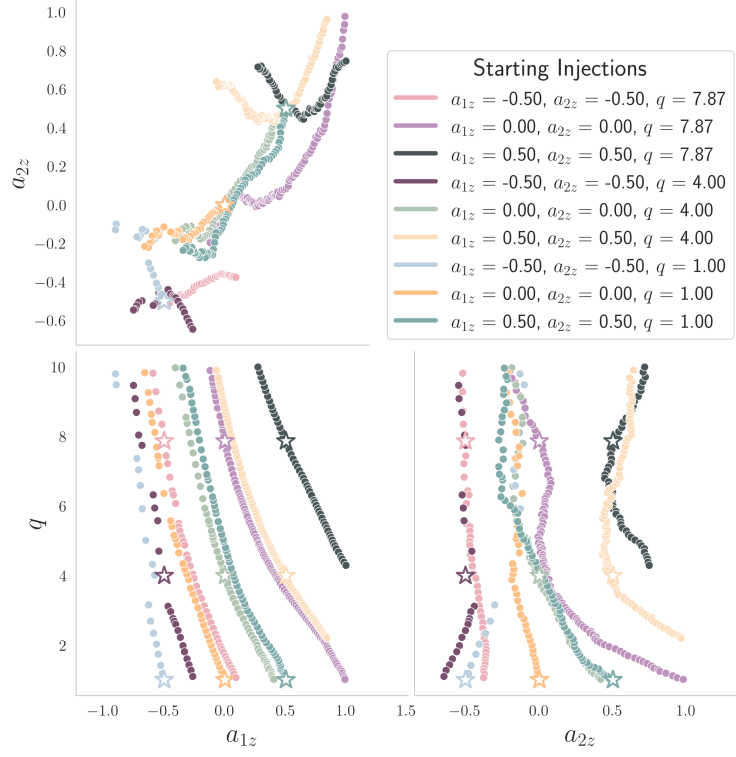


FIG. 7: Path mapped in  $q, a_{1z}, a_{2z}$  for nine distinct starting reference simulation: stars indicate the starting reference simulation

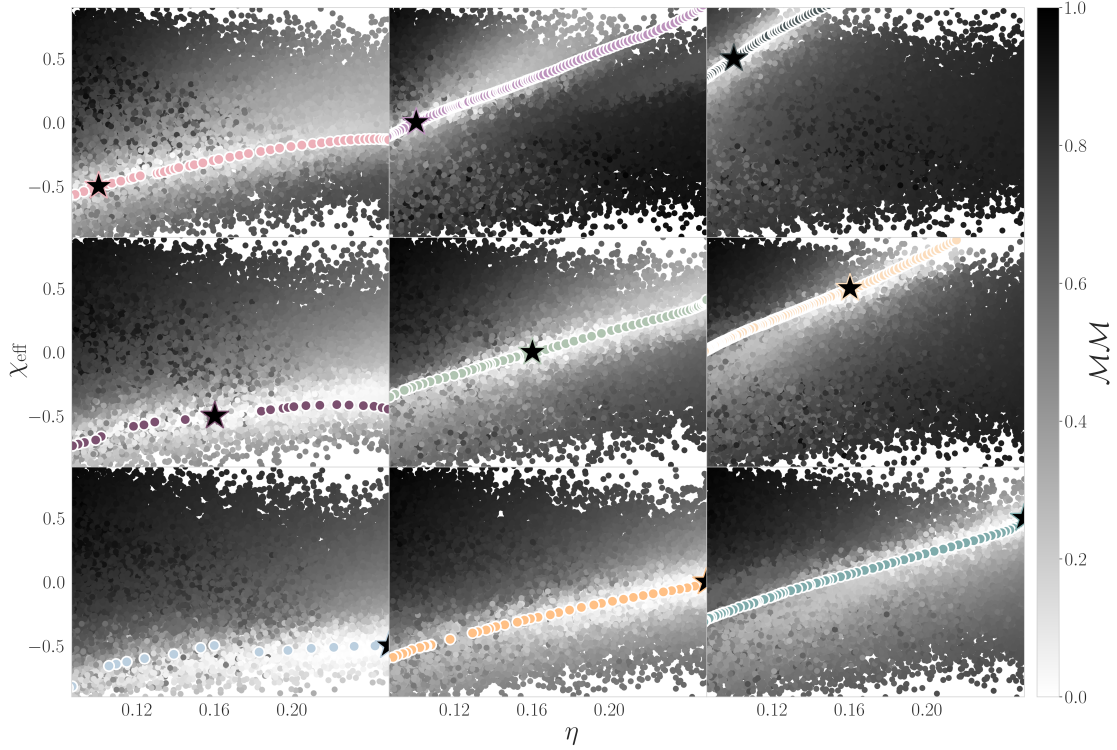


FIG. 8: Mapped path in Fig. 7 projected over  $\chi_{\text{eff}} - \eta$  plane.

degrees of freedom  $q, a_1, a_2, \theta_1, \theta_2$ . The purpose of including spin angles stems from their typical ambiguity in LIGO detections, making them a significant factor when aiming for a more complete understanding of precessing waveforms; incorporating spin tilts is also crucial from an astrophysical perspective, as they shed light on the complex interactions and evolutionary pathways of merging binary systems, providing insights into the environments in which these systems formed and evolved. In this expanded analysis, we initiated tests based on two sets of initial parameters: the first set with varying equal spin magnitudes with constant mass ratios  $q = 2$  and spin angles  $\theta_1 = \theta_2 = 0$  (Figs. 9 and 10), and the second set with varying mass ratios with constant spin magnitudes (Figs. 11 and 12).

The correlations recovered from injections with different spin magnitudes seem to be shifted linearly for different starting injections. We observe that  $a_2, \theta_1$  and  $a_2, \theta_2$  are not correlated, as expected. However, there seems to be a strong linear correlation between  $q, \theta_1$  and  $q, \theta_2$ .  $a_1$  seems to be correlated with other parameters whereas  $a_2$  seems to be uncorrelated (horizontal and vertical plot traces). The overplot seems to deviate from the degenerate region at the boundary of the mapping. Future work includes verifying whether this behavior comes from the mapping algorithm or is a valid correlation that does not appear in the  $\chi_{\text{eff}} - \eta$  plane.

The results from injections of varying mass ratios seem more complex, though the overplot verifies that the correlation is accurate on the  $\chi_{\text{eff}} - \eta$  plane. It is worth noticing that the mapper does not span across the  $\chi_{\text{eff}} - \eta$  space for more asymmetric mass ratios.

## V. CONCLUSION AND FUTURE WORK

In this study, we introduced a comprehensive methodology for mapping parameter correlations in precessing binary black hole (BBH) signals, extending the neural network framework proposed in Ferguson [7]. Utilizing data from the SXS catalog [16], our model specializes in predicting the mismatch of gravitational waveforms in the  $l = 2, m = 2$  modes. We confirmed the efficacy of our approach by projecting the discovered correlations onto the  $\chi_{\text{eff}} - \eta$  plane, where they align well with the known linear degeneracies. While our results demonstrate strong agreement with  $\chi_{\text{eff}} - \eta$  relation, there are observed deviations at the boundaries of the parameter space that require further exploration.

In terms of ongoing and future work, we trained the neural network with the `NRSur7dq4` waveform model to include higher-order modes [17]. This is particularly important for understanding events similar to GW190521, which involve high-mass, highly precessing systems. Additionally, we are in the process of training a network on the `IMRPhenomXPHM` [18] waveform for low-mass systems (detector frame  $M = 30 M_{\odot}$ ). Our future goals include conducting detailed analyses on events resembling GW190521 and making comparative studies across neural networks trained on different detector frame masses.

## VI. ACKNOWLEDGEMENTS

This work was supported by the National Science Foundation grant PHY-2150027, as part of the LIGO Laboratory Summer Undergraduate Research Fellowship program (NSF REU), and the California Institute of Technology Student-Faculty Programs (SFP). I am grateful for the guidance and support provided by my mentors Simona Miller, Katerina Chatziioannou, and Deborah Ferguson, with a special acknowledgment to Deborah for developing the network used for this research.

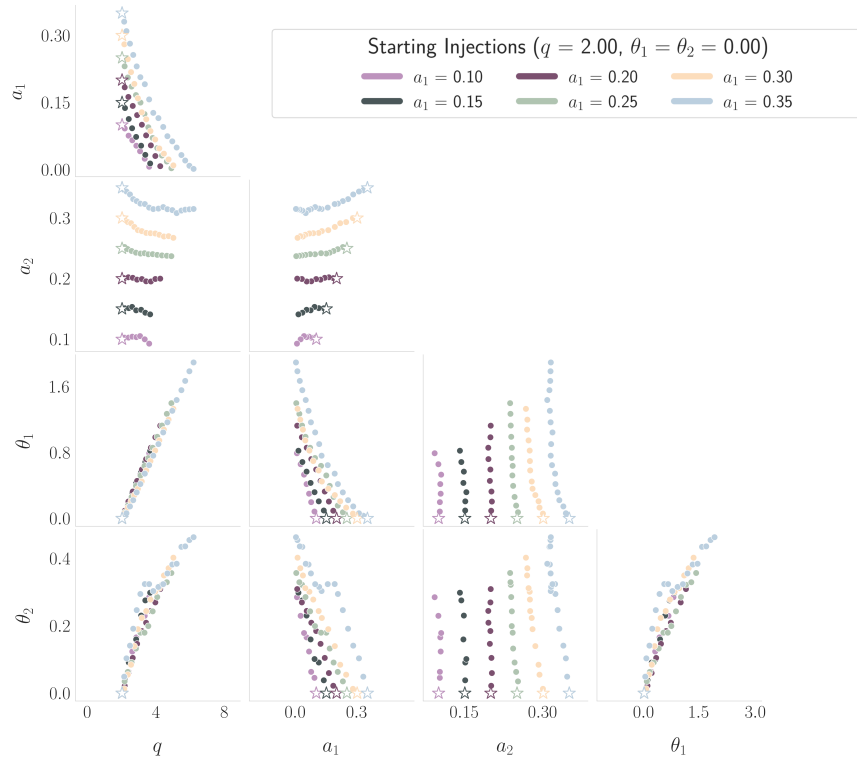


FIG. 9: Path mapped in  $q, a_1, a_2, \theta_1, \theta_2$  for reference simulation of varying spin magnitudes.

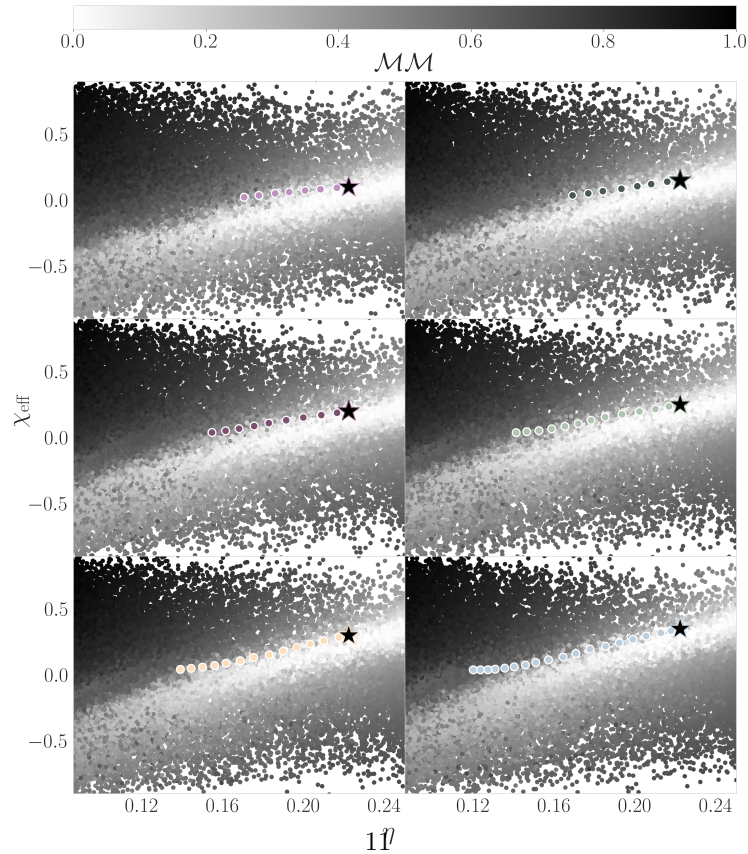


FIG. 10: Mapped path in Fig. 9 projected over  $\chi_{\text{eff}} - \eta$  plane.

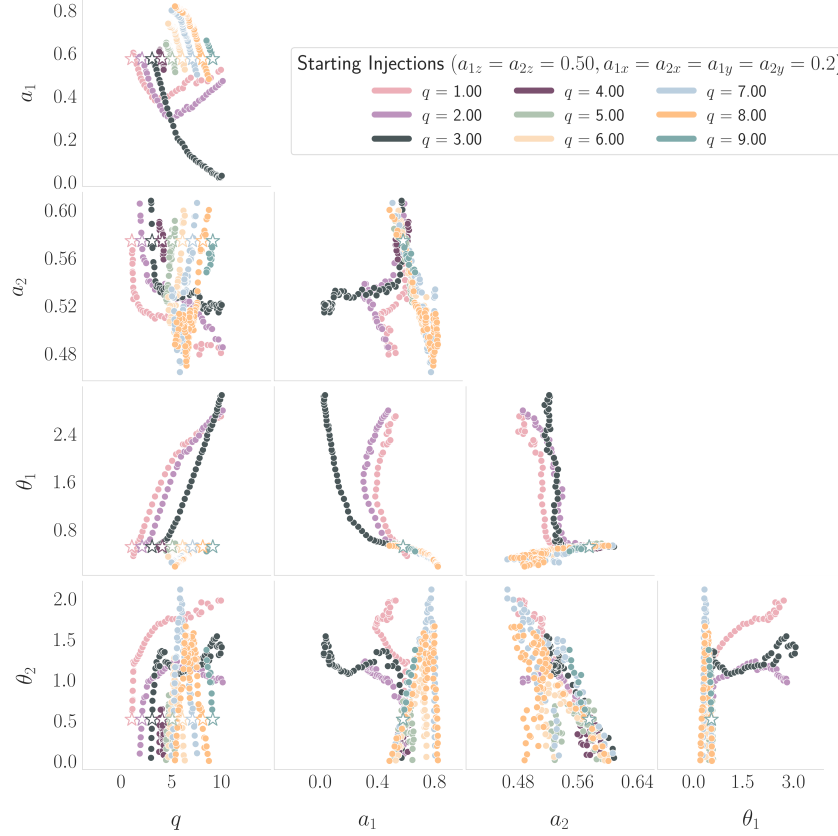


FIG. 11: Path mapped in  $q, a_1, a_2, \theta_1, \theta_2$  for reference simulation of varying mass ratios.

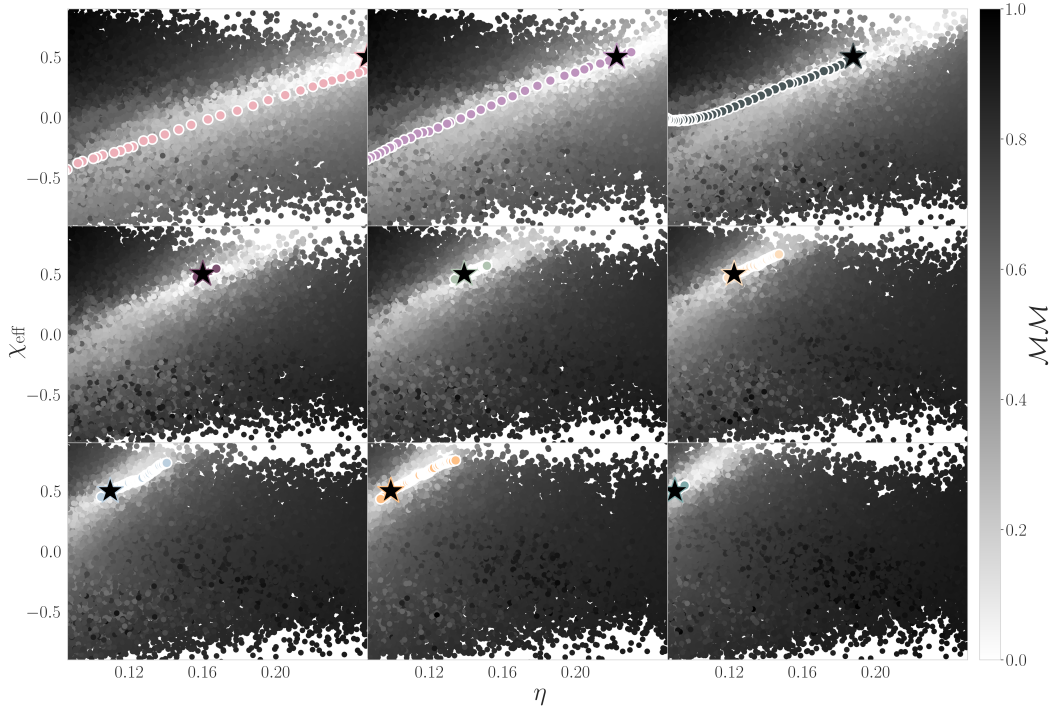


FIG. 12: Mapped path in Fig. 11 projected over  $\chi_{\text{eff}} - \eta$  plane.

## Appendix A: Degenerate Waveforms

In the study of binary black hole (BBH) waveforms, certain combinations of parameters may yield signals that are nearly indistinguishable when viewed through detectors. We focus our attention on a series of

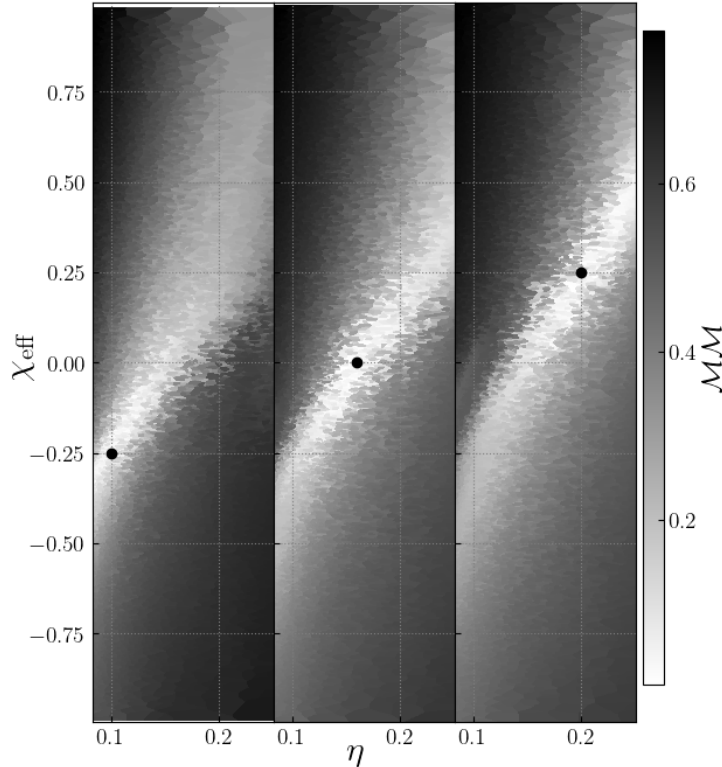


FIG. 13: Reference simulations chosen at  $\chi_{\text{eff}} = -0.25, 0, 0.25$  and  $\eta = 0.1, 0.16, 0.2$  along the line where the two parameters are approximately degenerate. The degeneracy exhibited is globally consistent for the points chosen with some local variations due to SNR.

reference simulations, as shown in Fig. 13, at various points along the line where the effective spin parameter  $\chi_{\text{eff}}$  and the symmetric mass ratio  $\eta$  are approximately degenerate. When waveforms are degenerate, any parameter space generated around them should exhibit a similar structure. In other words, degenerate waveforms would map onto almost identical regions in the parameter space, assuming the effect of noise is minimal or appropriately accounted for. However, it's crucial to note that while the global behavior is generally consistent, there may be local variations due to factors such as the signal-to-noise ratio (SNR). The concept of waveform degeneracy is essential for understanding the uncertainties associated with parameter estimation.

## Appendix B: Gaussian Mixture Model (GMM)

In this section, we detail the method utilized for local estimation of a single Gaussian distribution from multidimensional data through the `sklearn.mixture` implementation. The Gaussian Mixture Model (GMM) is a probabilistic model representing a mixture of multiple Gaussian distributions. Through the `sklearn.mixture` framework, we apply the GMM to fit data points in our BBH parameter space. The foundational assumption of this model is that the observed data is generated from multiple Gaussian distributions. Each component of the GMM, or cluster, is defined by its mean ( $\mu_k$ ) and covariance matrix

$(\Sigma_k)$ :

$$p(\mathbf{x} \mid \boldsymbol{\mu}_k, \boldsymbol{\Sigma}_k) = \mathcal{N}(\boldsymbol{\mu}_k, \boldsymbol{\Sigma}_k) = (2\pi)^{-\frac{D}{2}} |\boldsymbol{\Sigma}_k|^{-\frac{1}{2}} \exp\left(-\frac{1}{2}(\mathbf{x} - \boldsymbol{\mu}_k)^\top \boldsymbol{\Sigma}_k^{-1}(\mathbf{x} - \boldsymbol{\mu}_k)\right)$$

We used the Bayesian approach `sklearn.mixture.BayesianGaussianMixture` integrated in the module to counteract overfitting issues, especially when a GMM with a single component is used. This is represented using Bayes' theorem:

$$p(\theta \mid d) = \frac{\mathcal{L}(d \mid \theta)\pi(\theta)}{\mathcal{Z}(d)}$$

Gaussian Mixture Models uses an Expectation - Maximization (EM) Algorithm for parameter estimation. The likelihood function for GMM, which offers insight into the probability of observed data given our model parameters, is expressed as:

$$p(\mathbf{X} \mid \boldsymbol{\theta}) = \prod_{n=1}^N \sum_{k=1}^K \pi_k \frac{1}{\sqrt{2\pi\boldsymbol{\Sigma}_k}} \exp\left(-\frac{(\mathbf{x}_n - \boldsymbol{\mu}_k)^\top \boldsymbol{\Sigma}_k^{-1}(\mathbf{x}_n - \boldsymbol{\mu}_k)}{2}\right),$$
$$\mathcal{L} = \log p(\mathbf{X} \mid \boldsymbol{\theta}) = \sum_{n=1}^N \log \left[ \sum_{k=1}^K \pi_k \frac{1}{\sqrt{2\pi\boldsymbol{\Sigma}_k}} \exp\left(-\frac{(\mathbf{x}_n - \boldsymbol{\mu}_k)^\top \boldsymbol{\Sigma}_k^{-1}(\mathbf{x}_n - \boldsymbol{\mu}_k)}{2}\right) \right].$$

Here,  $\boldsymbol{\theta}$  encapsulates the full set of model parameters, and the function  $\mathcal{L}$  denotes the log-likelihood, crucial for the iterative optimization within the EM algorithm.

### Appendix C: Comparison of Methods

We verified the effectiveness of these methods on dummy 2D data, supplemented with a Gaussian value in the third dimension, using a defined covariance matrix and mean with noise introduced. The fits are shown in Fig. 15. Fig. 14a and 14b show that the results from the two methods are consistent (near identical) for `n.components = 1` for GMM and `n.components = 2` for PCA in a two-dimensional parameter space.

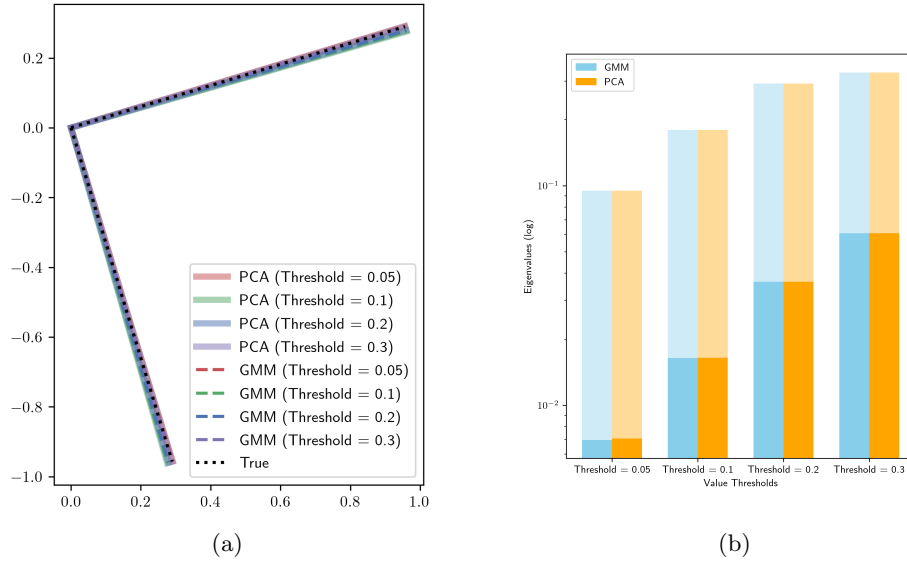


FIG. 14: Comparisons of GMM and PCA results. (a) Eigenvectors. (b) Eigenvalues.

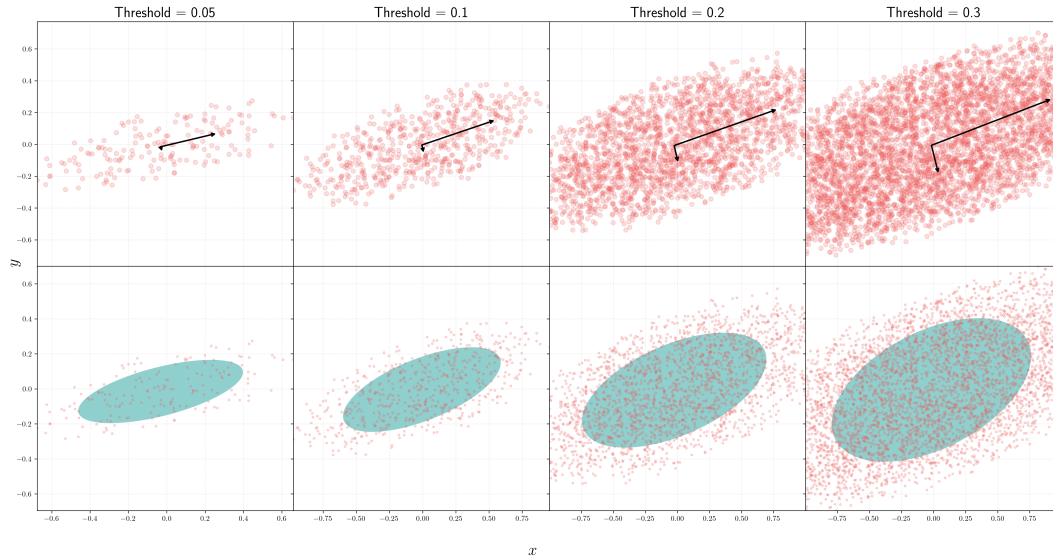


FIG. 15: Comparison between modeling the distribution with PCA (top) and GMM (bottom): principal components in black arrows, scaled for best visualization, means and covariance plotted as ellipse.

- 
- [1] R. Abbott, T. D. Abbott, S. Abraham, F. Acernese, K. Ackley, C. Adams, R. X. Adhikari, V. B. Adya, C. Affeldt, M. Agathos, et al., *The Astrophysical Journal* **900**, L13 (2020), URL <https://doi.org/10.48550/arXiv.2009.01190>.
- [2] I. Mandel and A. Farmer, *Physics Reports* **955**, 1 (2022), URL <https://doi.org/10.48550/arXiv.1806.05820>.
- [3] S. Biscoveanu, M. Isi, V. Varma, and S. Vitale, *Physical Review D* **104** (2021), URL <https://doi.org/10.1103/2Fphysrevd.104.103018>.
- [4] R. O’Shaughnessy, L. London, J. Healy, and D. Shoemaker, *Physical Review D* **87** (2013), URL <https://doi.org/10.1103/2Fphysrevd.87.044038>.
- [5] B. J. Owen, *Phys. Rev. D* **53**, 6749 (1996), URL <https://link.aps.org/doi/10.1103/PhysRevD.53.6749>.
- [6] S. D. Mohanty, *Phys. Rev. D* **57**, 630 (1998), URL <https://link.aps.org/doi/10.1103/PhysRevD.57.630>.
- [7] D. Ferguson, *Physical Review D* **107** (2023), URL <https://doi.org/10.48550/arXiv.2209.15144>.
- [8] P. Schmidt, F. Ohme, and M. Hannam, *Phys. Rev. D* **91**, 024043 (2015), URL <https://link.aps.org/doi/10.1103/PhysRevD.91.024043>.
- [9] C. Cutler and É. E. Flanagan, *Physical Review D* **49**, 2658 (1994), URL <https://doi.org/10.1103/2Fphysrevd.49.2658>.
- [10] E. Poisson and C. M. Will, *Physical Review D* **52**, 848 (1995), ISSN 0556-2821, arXiv:gr-qc/9502040, URL <http://arxiv.org/abs/gr-qc/9502040>.
- [11] K. K. Y. Ng, S. Vitale, A. Zimmerman, K. Chatziioannou, D. Gerosa, and C.-J. Haster, *Physical Review D* **98**, 083007 (2018), ISSN 2470-0010, 2470-0029, arXiv:1805.03046 [astro-ph, physics:gr-qc], URL <http://arxiv.org/abs/1805.03046>.
- [12] M. Pürrer, *Classical and Quantum Gravity* **31**, 195010 (2014), ISSN 0264-9381, 1361-6382, arXiv:1402.4146 [gr-qc], URL <http://arxiv.org/abs/1402.4146>.
- [13] A. Nitz, I. Harry, D. Brown, C. M. Biwer, and J. Willis, *gwastro/pycbc: v2.4.0 release of pycbc* (2023), URL <https://doi.org/10.5281/zenodo.10013996>.
- [14] K. Wette, *SoftwareX* **12**, 100634 (2020), URL <https://doi.org/10.1016/2Fj.softx.2020.100634>.
- [15] V. Varma, S. E. Field, M. A. Scheel, J. Blackman, D. Gerosa, L. C. Stein, L. E. Kidder, and H. P. Pfeiffer, *Phys. Rev. Res.* **1**, 033015 (2019), URL <https://link.aps.org/doi/10.1103/PhysRevResearch.1.033015>.
- [16] M. Boyle, D. Hemberger, D. A. B. Iozzo, G. Lovelace, S. Ossokine, H. P. Pfeiffer, M. A. Scheel, L. C. Stein, C. J. Woodford, A. B. Zimmerman, et al., *Classical and Quantum Gravity* **36**, 195006 (2019), ISSN 0264-9381, 1361-6382, arXiv:1904.04831 [astro-ph, physics:gr-qc], URL <http://arxiv.org/abs/1904.04831>.
- [17] V. Varma, S. E. Field, M. A. Scheel, J. Blackman, D. Gerosa, L. C. Stein, L. E. Kidder, and H. P. Pfeiffer, *Physical Review Research* **1**, 033015 (2019), publisher: American Physical Society, URL <https://link.aps.org/doi/10.1103/PhysRevResearch.1.033015>.
- [18] G. Pratten, C. García-Quirós, M. Colleoni, A. Ramos-Buades, H. Estellés, M. Mateu-Lucena, R. Jaume, M. Haney, D. Keitel, J. E. Thompson, et al., *Phys. Rev. D* **103**, 104056 (2021), URL <https://link.aps.org/doi/10.1103/PhysRevD.103.104056>.